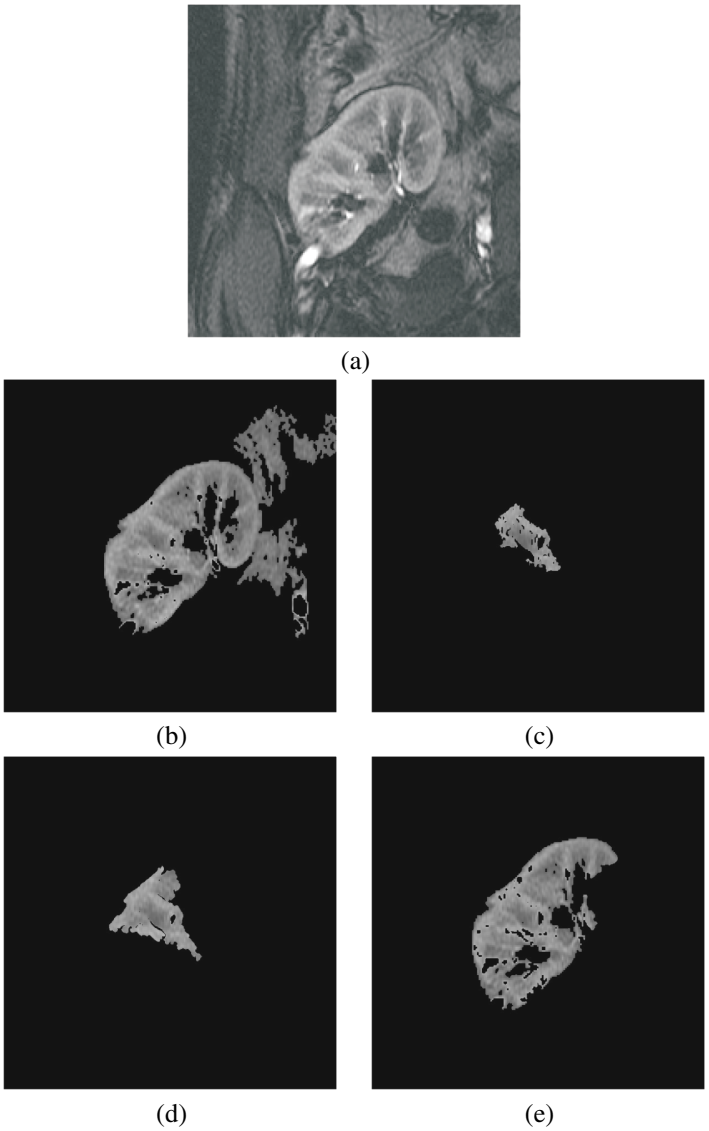

Figure 1. (a) Kidney to be segmented from the surrounding organs. The results of some popular segmentation algorithms that depend only on gray-level and gradient information, (b) connected thresholding, (c) fast marching level sets, (d) geodesic active contours, and (e) thresholding level sets segmentation.

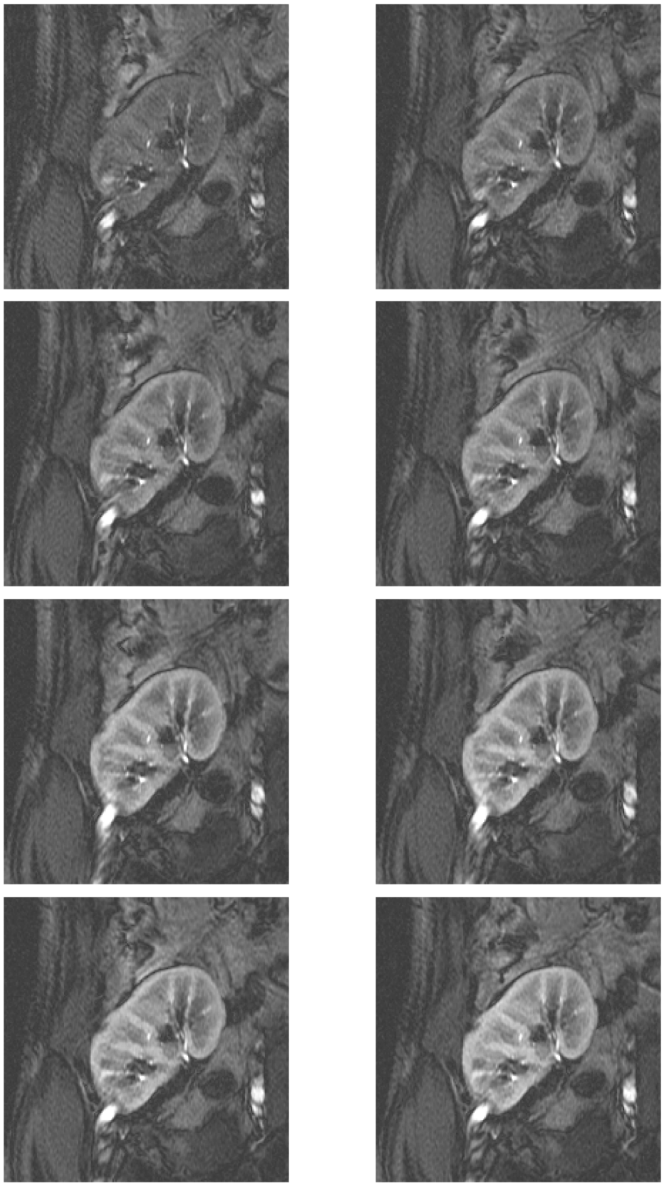

Figure 2. Example of a DCE-MRI series. For each patient, 150 images are taken from one cross-section with 4-second intervals. Eight of one subject (numbers 1, 4, 5, 6, 10, 15, 21, 27) are shown here to give an idea of the protocol.

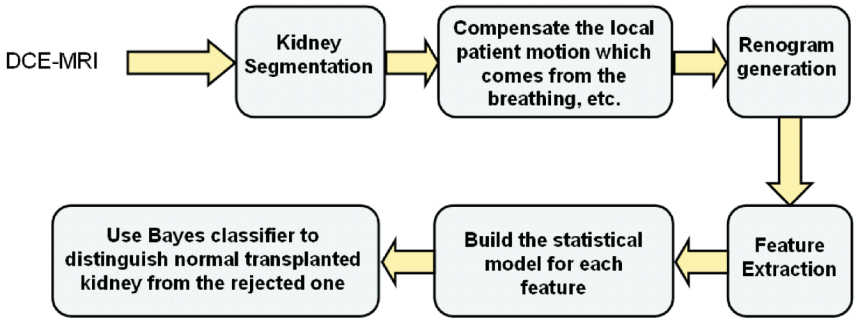

Figure 3. Block diagram of the proposed image analysis to create a CAD system for renal transplantation.

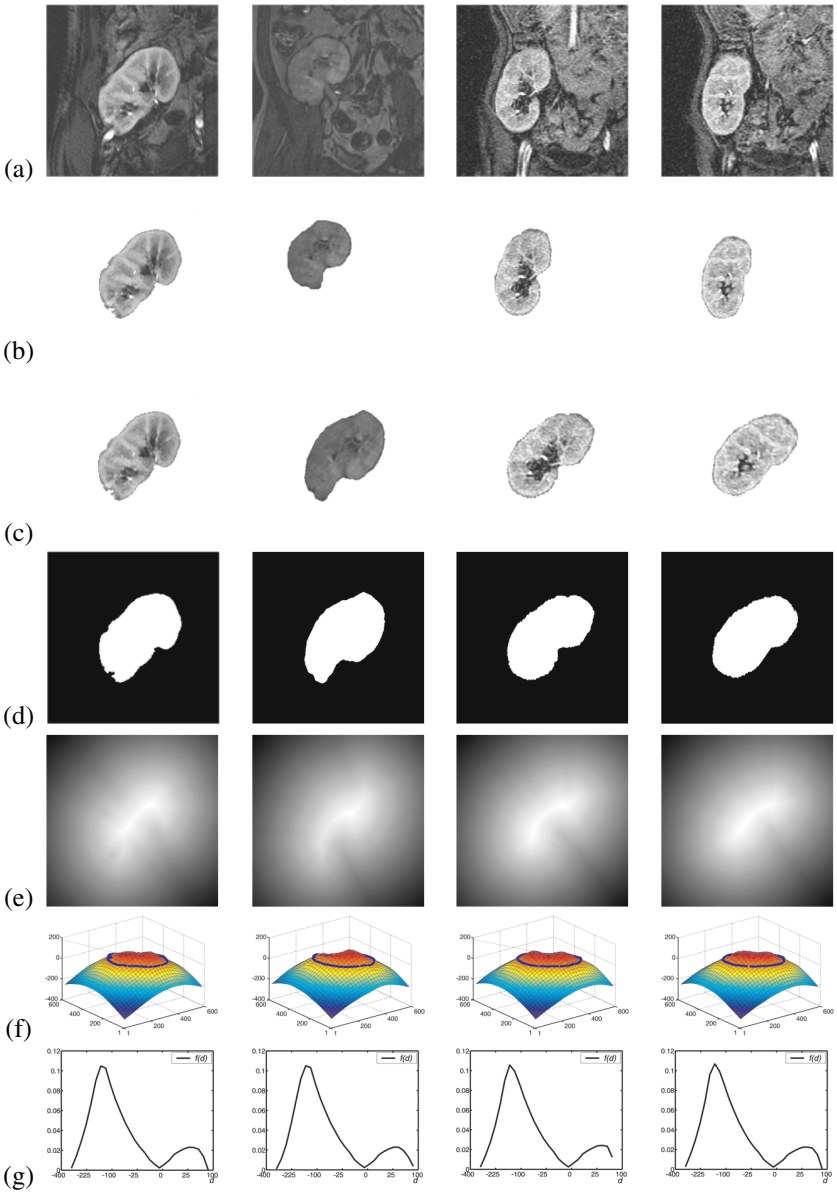

Figure 4. Steps of shape reconstruction. Samples of the database (a), manual segmentation results (b), affine mutual information registration (c), binarization (d), signed distance maps (e), level sets functions (f), and the empirical densities of signed distance maps (g).

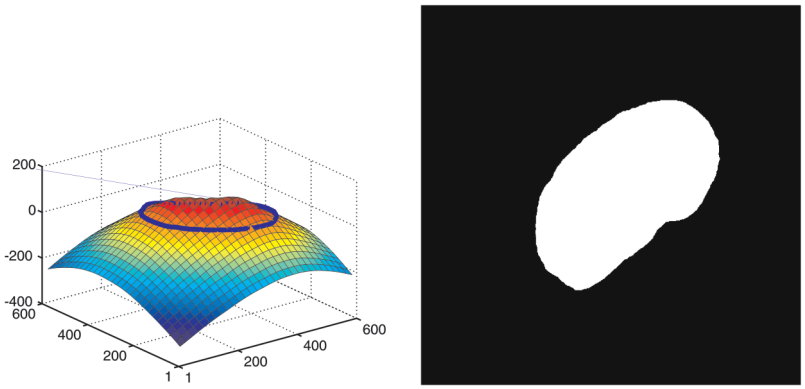

Figure 5. Average signed distance map for the kidney object (a), and the average shape of the kidney after thresholding the average signed distance map from the zero level (b).

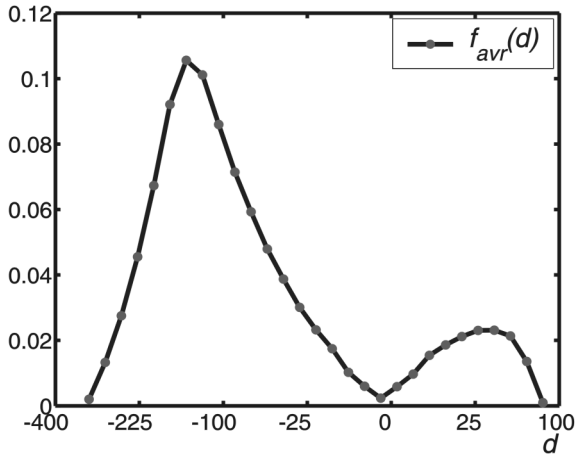

Figure 6. Average empirical signed distance map density representing the shape. It is calculated as the average empirical density of empirical densities shown in Figure 4g. The positive distances indicate the kidney area, while the negative distances indicate the background.

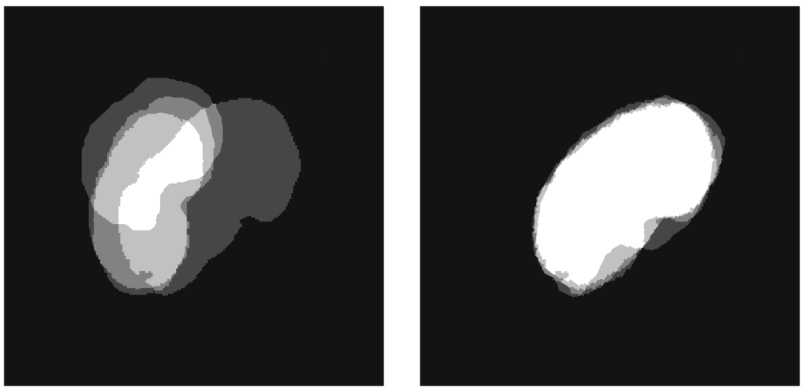

(a) (b)

Figure 7. Comparison of the shape overlaps in the training data sets before (a) and after (b) alignment.

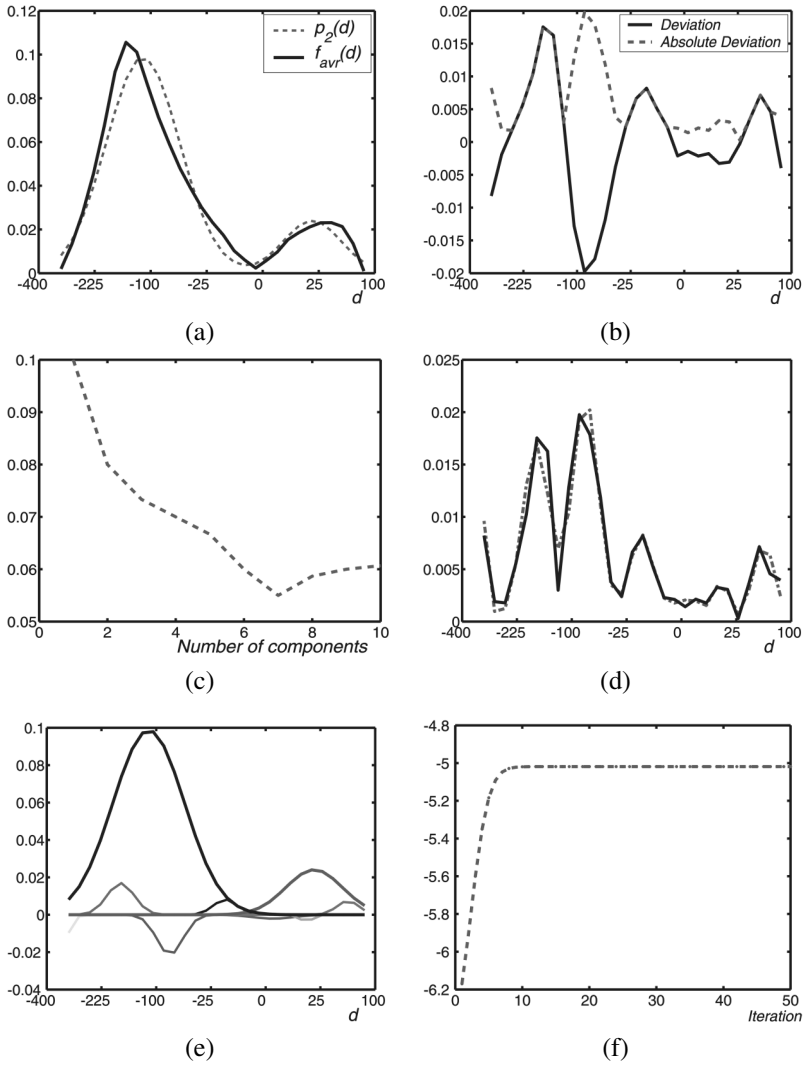

Figure 8. Estimated two dominant modes that present the kidney area and its background (a); the scaled-up absolute deviation of the approximation and its LCDG model (b); approximation error for the scaled absolute deviation as a function of number of subordinate Gaussians (c); density estimation of the scaled-up absolute deviation (d); final LCDG model (e); and log-likelihood changes at the EM iterations (f).

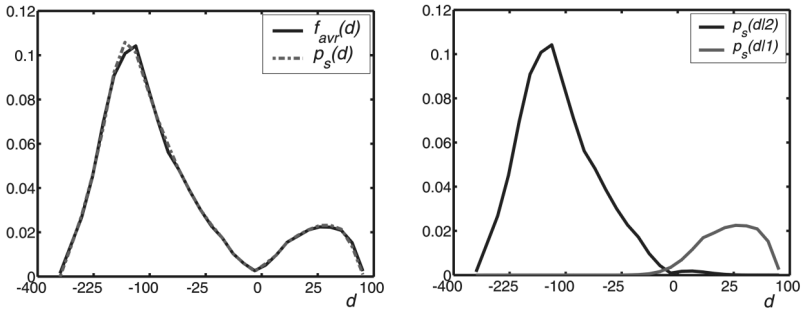

Figure 9. Final two-class LCDG approximation of the mixed density (a); and final LCDG models for each class (b).

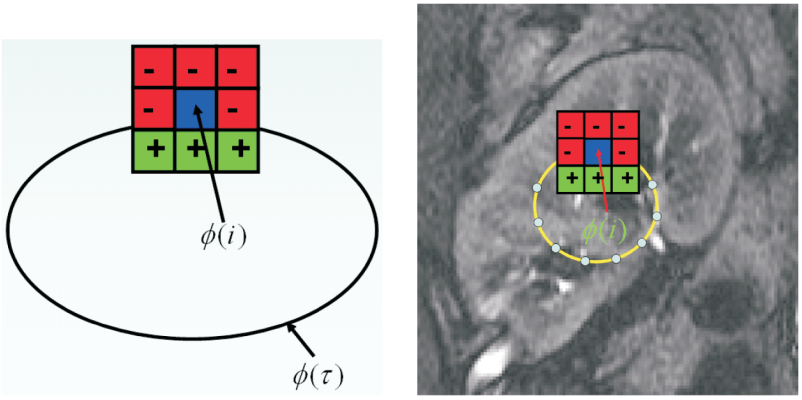

Figure 10. Greedy propagation of the deformable model (a). The deformable model in (a) is initialized in the given kidney to be segmented (b).

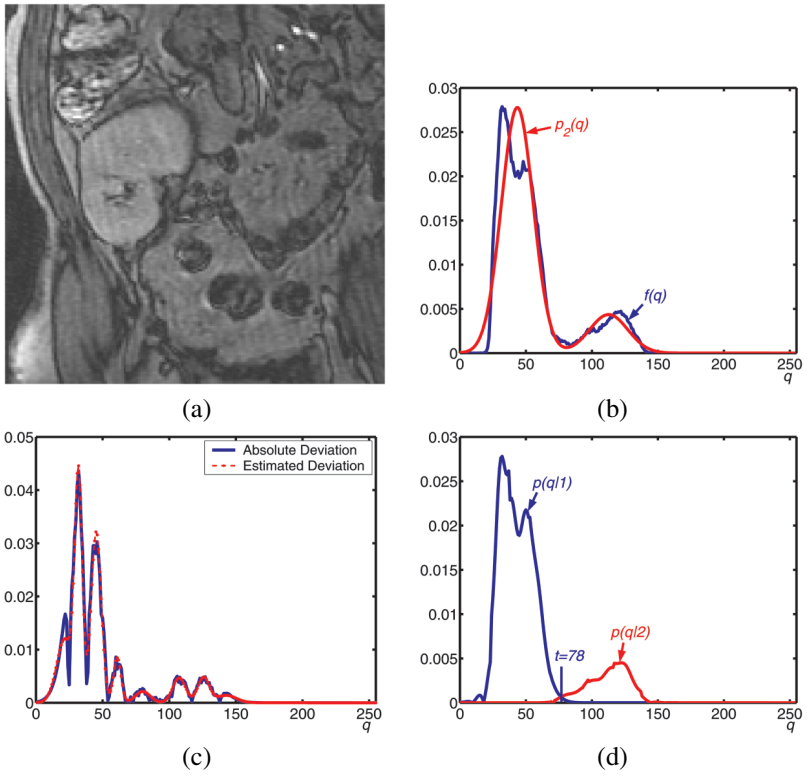

Figure 11. Initial LCDG model of the bimodal empirical gray-level distribution: the DMRI slice (a), its empirical gray-level distribution approximated with the dominant mixture of the DGs (b), the scaled-up absolute deviation of the approximation and its LCDG model (c), and the LCDG model of each class (d) for the best separating threshold $t = 78$.

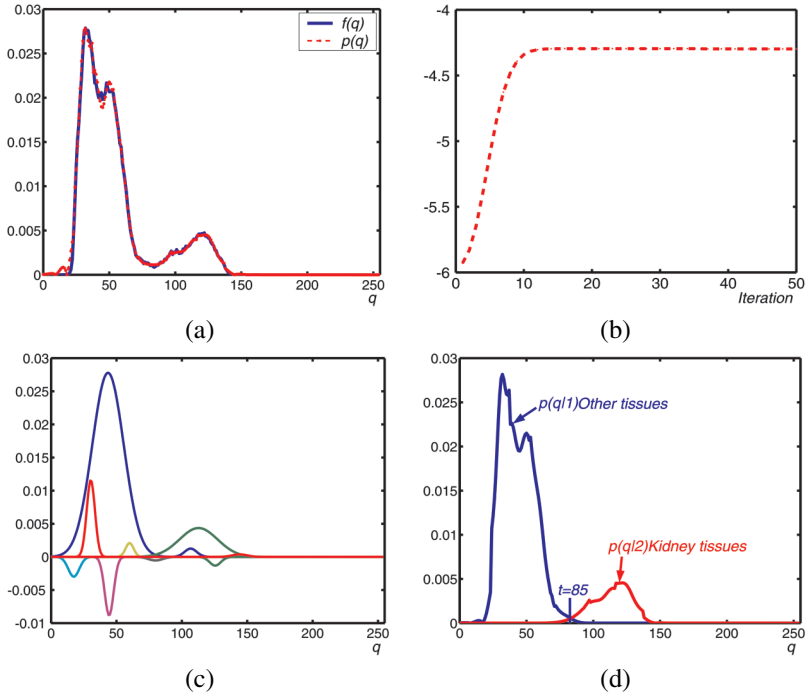

Figure 12. Final 2-class LCDG model (a), log-likelihood changes at the EM iterations (b), ten components of the final LCDG (c), the final LCDG model of each class for the best separating threshold $t = 85$ (d).

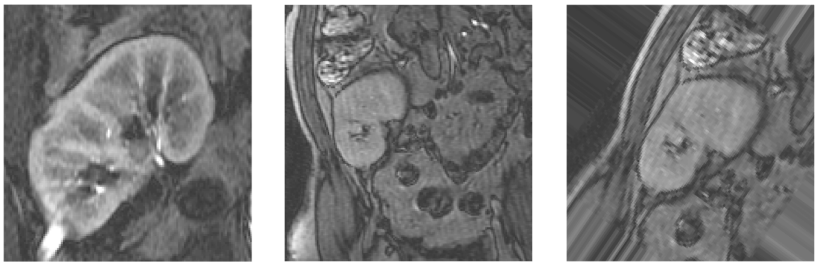

Figure 13. Kidney from the aligned database (a); a kidney to segment (b); alignment of (a) and (b) using affine mutual information registration (c).

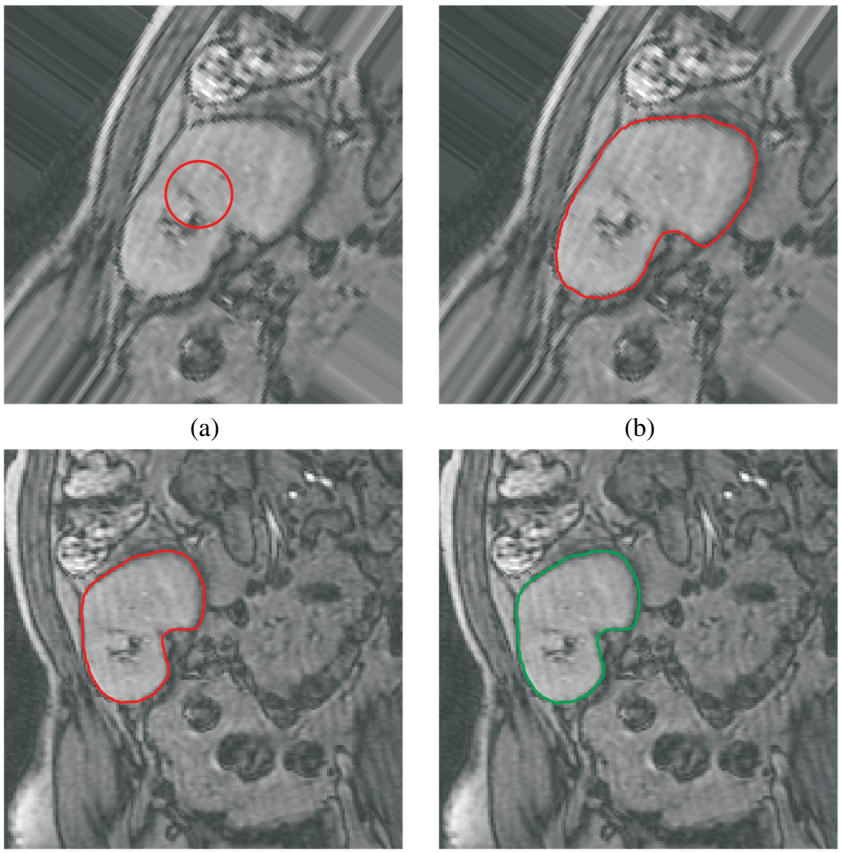

Figure 14. Initialization of deformable model (a); final segmentation of the aligned image (b); final segmentation (c) after multiplying the aligned image by inverse transformation (error = 0.23%); and radiologist segmentation (d).

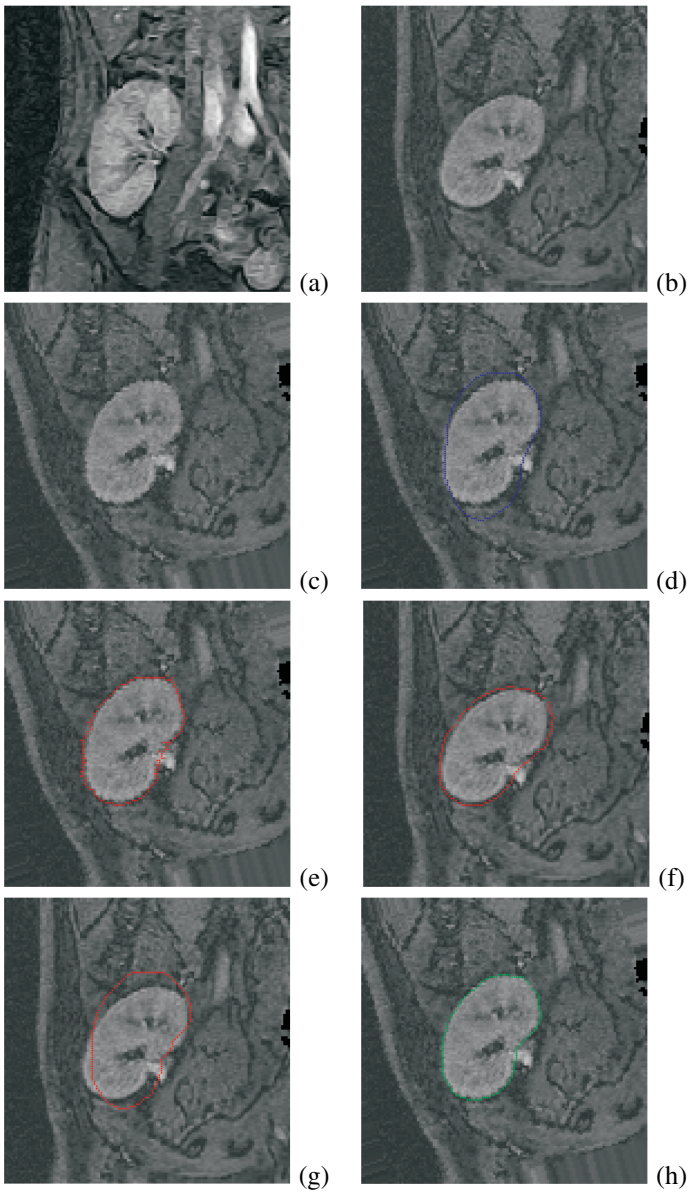

Figure 15. Chosen training kidney prototype (a); an image to be segmented (b); its alignment to the prototype (c); the contour of the training prototype superimposed on the aligned test image (d); the segmentation result (e); the same result (f) after its inverse affine transform to the initial image (b) (total error 0.63% in comparison to ground truth (h); the final boundary and the ground truth are in red and green, respectively), and the segmentation (g) with the algorithm in [60] (the total error 4.9% in comparison to ground truth (h)).

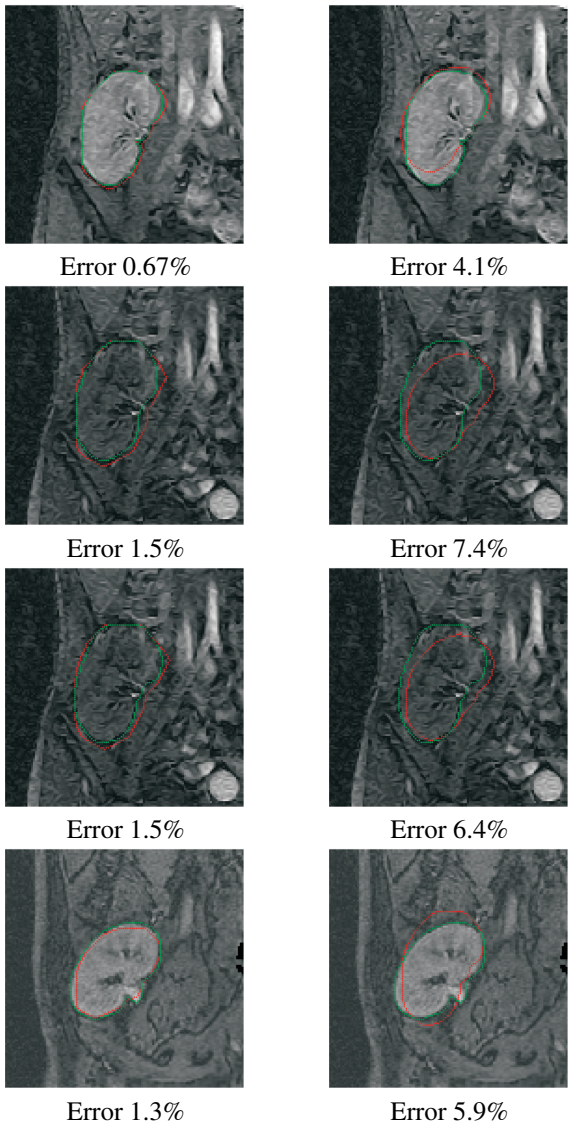

Figure 16. Segmentation of four other kidney DCE-MR images: the left column — our final boundaries and the ground truth (in red and green, respectively); the right column — the segmentation with the algorithm in [60] vs. the ground truth (in red and green, respectively).

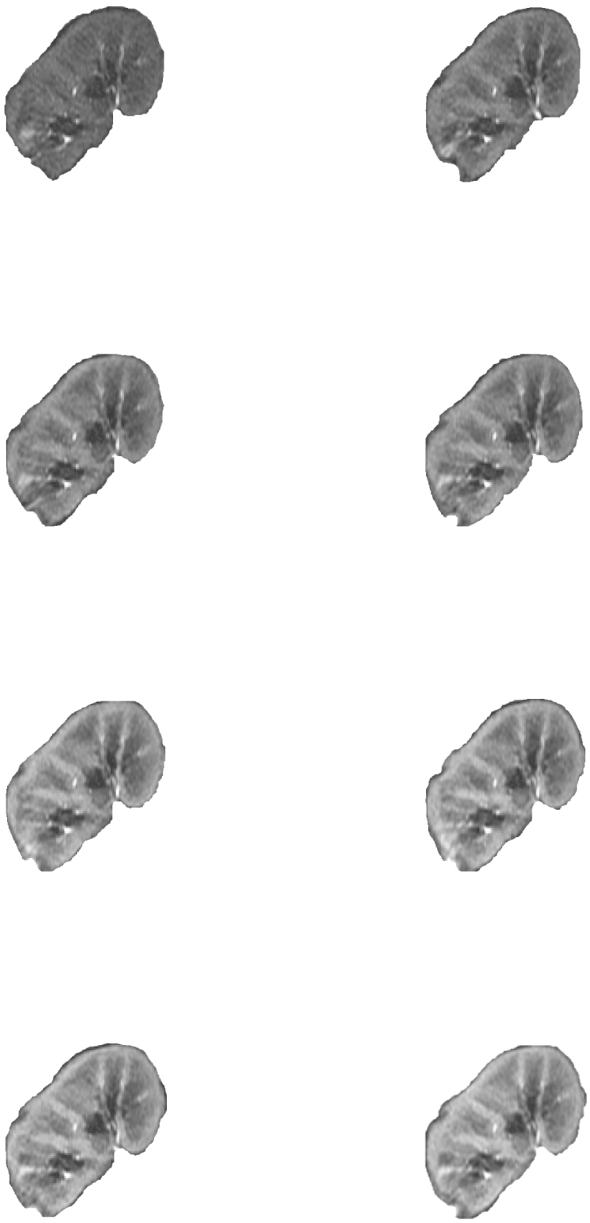

Figure 17. Segmentation results of a DCE-MRI series, a part of which was shown in Figure 2.

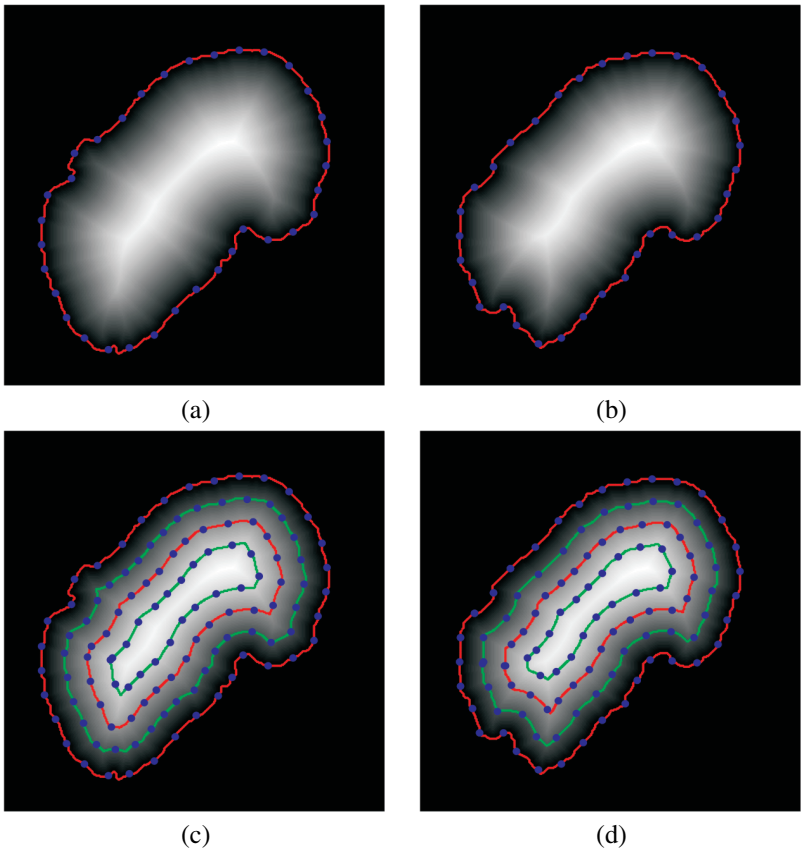

Figure 18. Distance map of two kidneys (a, b) and the samples of isocontours (c, d).

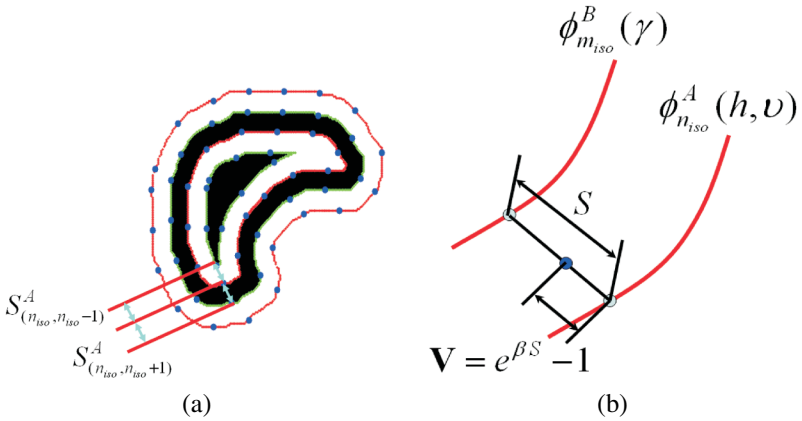

Figure 19. Model constraints (a), and model evolution (b).

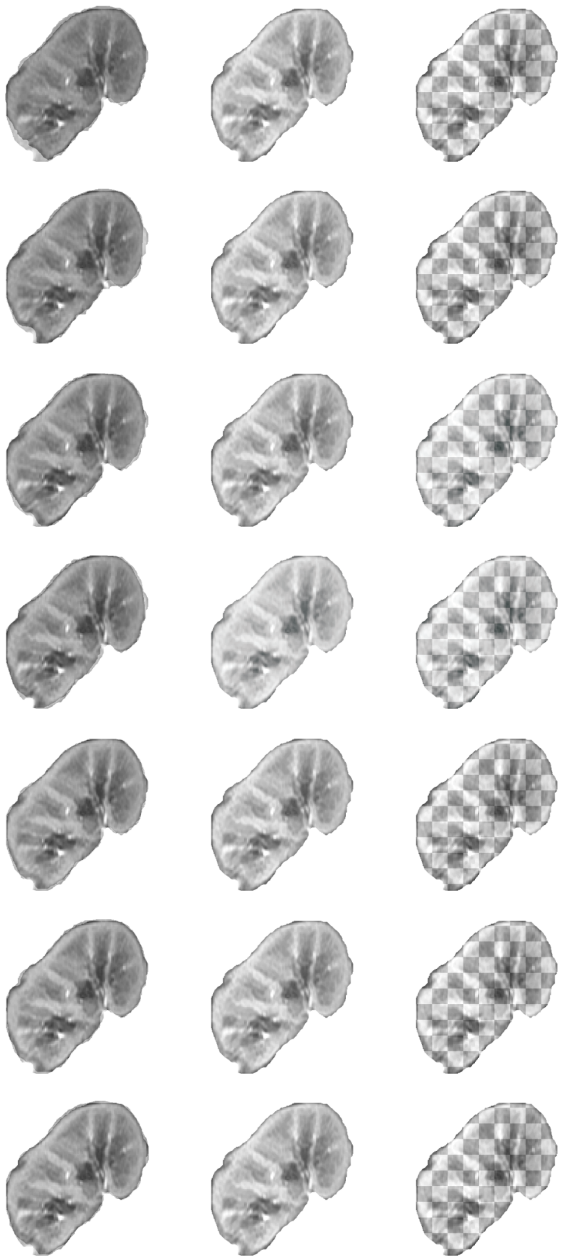

Figure 20. Example of a DCE-MRI series after nonrigid registration.

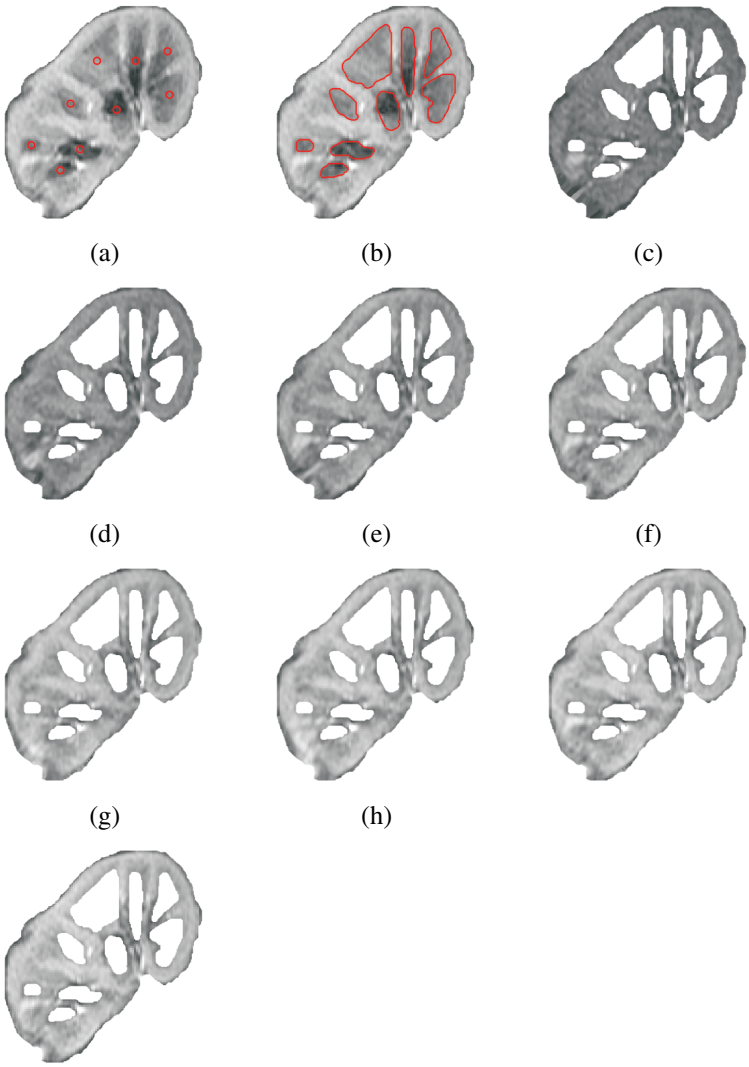

Figure 21. Segmentation of the cortex from kidney images. Several medullary seeds are initialized (a), and the deformable model grows from these seed points (b). After the medulla is extracted from the kidney, the cortex is propagated over the whole sequence of images, as shown in (c)-(h).

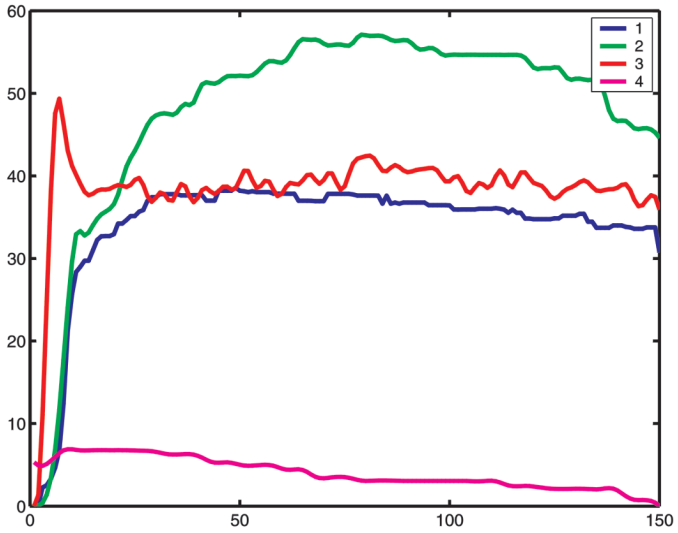

Figure 22. Cortex intensity vs. scan number from 4 subjects. There are 4 seconds between each scan. Subjects 1 and 2 have acute rejection, subject 3 is normal, and subject 4 is chronic glomerulopathy proved by biopsy. In these cortical renograms the normal patient shows the expected abrupt increase in intensity along with a fast decrease, followed by a constant valley and a slow decrease. On the other hand, these abrupt patterns are not seen in acute rejection patients; there is no definite peak, and the time to reach peak intensity is delayed. Subject 4 shows that DCE-MRI is also powerful in distinguishing other diseases.